Sputtering Effects and Water Formation on an Amorphous Silicate Surface

ARTICLE *in* THE JOURNAL OF PHYSICAL CHEMISTRY A · MARCH 2013

Impact Factor: 2.69 · DOI: 10.1021/jp312816k · Source: PubMed

THE JOURNAL OF PHYSICAL CHEMISTRY A

Article

pubs.acs.org/JPCA

Sputtering Effects and Water Formation on an Amorphous Silicate Surface

Dapeng Jing,[†] Jiao He,[†] Massimo Bonini,[‡] John R. Brucato,[§] and Gianfranco Vidali*[,†]

[†]Physics Department, 201 Physics Bldg., Syracuse University, Syracuse, New York 13244-1130, United States

[‡]INAF - Astrophysical Observatory of Arcetri, L.go E. Fermi 5, 50125 Firenze, Italy

[§]Department of Chemistry, CSGI, via della Lastruccia, 3, 50019 Sesto Fiorentino (Firenze), Italy

ABSTRACT: We studied the formation of deuterated water on an amorphous silicate surface held at low temperature (10 K < T < 40 K). The surface is first characterized by using Ar^+ ion bombardment, and preferential sputtering of oxygen is found. Sputtering creates oxygen vacancies in the surface region that can be filled by deposition of atomic oxygen. The conditions used in the experiment are meant to make it relevant to the study of the initial stages of water formation on dust grains in interstellar space. By changing the D/O ratio of atomic beams of deuterium and oxygen at thermal energy and the temperature of the sample during deposition, we show that the routes to the formation of D_2O_2 can be untangled and, under certain circumstances, the net yield of D_2O_2 can be suppressed. The formation efficiency for water and other molecules is then estimated.

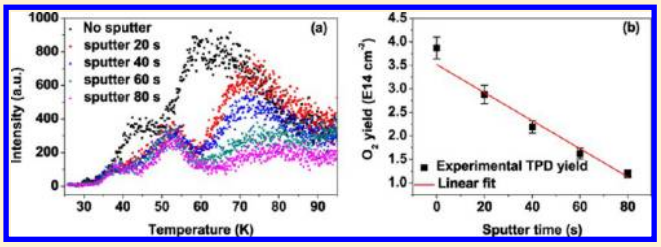

1. INTRODUCTION

The formation of water on surfaces is of obvious importance in chemical physics and astrophysics. Most of the experimental studies have been conducted on metal surfaces such as Pd, Pt, and Rh for which there is a large literature.[1−6] Water formation on ultrathin films of oxides on metals has also been studied.[7,8] In these cases, the strong interaction of either H or O, or both, with the metal or oxide surface drives the chemistry. On the other hand, little is known about the formation of water on Mg−Fe silicates. These silicates ($(Fe_xMg_{1-x})_2SiO_4$, $0 < x < 1$) along with carbonaceous materials are the two main types of dust present in interstellar space.[9] Dust grains, which have an average size of 0.1 μm, are eventually incorporated into protoplanetary disks from which planets emerge. In interstellar space, over 160 different types of molecules have been detected.[10] Many of these are formed in gas-phase reactions. However, some very important ones (e.g., H_2, H_2O, CO_2, CH_3OH, and H_2CO) are believed to form in significant amounts also on dust grains.[11,12] In the past few years, a number of experiments were carried out to study water formation on dust grain analogues or on ices. The reaction network to form water can be reduced to three channels: the hydrogenation of atomic oxygen, molecular oxygen and ozone.[13] These channels are described below.

Dulieu et al. used atomic hydrogen and oxygen on amorphous water ice to study the formation of H_2O at 10 K, as it occurs in dark clouds environments where dust grains are covered by ices.[14] Jing et al. used D and O beams deposited on an amorphous silicate (held at 15−25 K) to study the initial stages of formation of water on bare grains at the edge of dark clouds.[15] In both cases, water is formed as follows:

$$O + H \rightarrow OH \quad (1)$$

$$OH + H \rightarrow H_2O \quad (2)$$

Miyauchi et al.[16] and Ioppolo et al.[17] sent H on an O_2 ice to probe the following reactions:

$$O_2 + H \rightarrow HO_2 \quad (3)$$

$$HO_2 + H \rightarrow H_2O_2 \quad (4)$$

$$H_2O_2 + H \rightarrow H_2O + OH \quad (5)$$

Mokrane et al.[18] and Romanzin et al.[19] studied the reaction of H with O_3 deposited or grown on a cold substrate:

$$O_3 + H \rightarrow O_2 + OH \quad (6)$$

In some of these reactions, OH is produced. OH can also participate in other reactions that form water. Oba et al.[20,21] deposited OH radicals obtained from dissociation of H_2O and directed onto the sample from an atomic beam- on a substrate to study the following reactions:

$$OH + OH \rightarrow H_2O_2 \quad (7)$$

$$OH + OH \rightarrow H_2O + O \quad (8)$$

$$OH + H_2 \rightarrow H_2O + H \quad (9)$$

Limitations in the dissociation of H_2 and O_2 make the interpretation of results rather difficult because the sample is irradiated not only with H and O atoms but also with H_2 and O_2. For instance, in the case of oxygen, dissociation efficiency is typically in the 30−40% range. Undissociated O_2 reacts with O,

Received: December 28, 2012
Revised: March 9, 2013
Published: March 18, 2013

and O_3 is formed. Therefore, even in a simple experiment of irradiation of H and O on a bare surface, all the three channels are potentially active. For example, Jing et al. found that, besides water, hydrogen peroxide (H_2O_2) and ozone were formed on the surface of an amorphous silicate.[15] Similar results were obtained using H on O_2 ice, ^{17}OH + OH,[20] or hydrogenation of O_3.[19] However, hydrogen peroxide has only recently discovered in the ISM with abundances of less than 10^{-10} with respect to H_2.[22]

In this study, we show how the relative yield of the reaction products can be influenced by the relative abundance of reactants and by the condition of the surface. Therefore, the results from this investigation should be useful to better model the formation of water on dust grains in actual space environments. Moreover, these results transcend space applications because the study of hydrogenation reactions on disordered surfaces is of wide applicability in chemical physics. After the description of the experimental methods, we present results of the characterization of the amorphous silicate. Then we show that the products of the reaction between deuterium and oxygen on the surface are influenced by the D/O ratio and by the surface temperature.

2. EXPERIMENTAL SECTION

The thin film silicate sample is prepared using the electron beam physical vapor deposition (EB-PVD) technique. The heating source is an e-beam produced by thermionic emission of a tungsten filament. The e-beam can be accelerated up to 8 kV and bended by a controllable magnetic field. Such heating source has been selected for its capacity to reach temperatures up to 10,000 °C. To increase heating uniformity, the e-beam can be swiped by varying the bending magnetic field. The heating rate, and the consequent deposition rate, can be modified by changing the intensity of the e-beam (up to 3 kW). The uniformity of the thickness of the deposited film depends only on the distance from the source and the solid angle of the cloud intercepted by the substrate. Reactive deposition has been applied to control the stoichiometry during deposition. In the present experiment, an oxygen rich atmosphere in the deposition chamber induces a reoxidation of the vapor compensating the oxygen loss.

The water formation experiments are conducted in a separate ultra high vacuum (UHV) setup. Detailed description of the UHV setup can be found elsewhere.[15] The main chamber has a base pressure $<2 \times 10^{-10}$ Torr at 300 K. A triple-pass Hiden HAL/3F quadrupole mass spectrometer (QMS) is mounted on a rotary platform for temperature-programmed desorption (TPD) and beam flux and composition measurements. The sample is a 3 μm thick amorphous silicate thin film deposited on a 0.5 in. diameter gold coated copper disk. Its temperature can be varied from 8 to 500 K and is measured by a calibrated LakeShore silicon diode thermometer. The sample holder is separated from the coldfinger via a thermal switch (800 K stage by ADS) so the sample can be heated to high temperature while keeping the coldfinger temperature low. This minimizes the desorption of gases from the coldfinger. The sample is cleaned repeatedly by heating it to 400 K in vacuum during bakeout and prior to each experiment. In some cases, the sample is also cleaned by Ar^+ ion sputtering. The surface is judged clean by a blank TPD run in which no adsorbent is exposed to the surface and hence no desorption peak is observed. The two beamlines consist of three independently pumped stainless steel chambers separated by collimators with a diameter of 2 mm. Each beam is controlled by a flag in the third chamber (closest to the main chamber) and a mechanical chopper in the second chamber. A radio frequency (RF) dissociation source is attached to each beamline to generate deuterium and oxygen atoms from their parent molecules. D_2 and $^{18}O_2$ are used to distinguish them from residual H_2 and $^{16}O_2$ in the UHV setup.The atoms may be in an excited level when formed in the RF source. However, after many collisions with the Pyrex tube and PTFE nozzle they are thermalized to 300 K and should already be vibrationally and electronically in the ground state.[23]

The QMS detector can be placed directly in sight with the beamlines to measure beam flux and composition. The collimated beams have a radial spread diameter of 3 mm whereas the cross-beam QMS detector entrance diameter is 5 mm. Therefore, the entire beam passes through the detector ionization chamber and a signal (in units of counts per second) is measured. Next, the conversion factor (detector counts to number density of molecules) is calculated by flooding the main chamber with the target gas, where the number density of molecules in the chamber can be calculated from the chamber pressure. Ionization gauge gas correction factors of 0.35 for D_2 and of 1.0 O_2 are used because the ionization gauge is calibrated for N_2. When the RF sources are turned on, the deuterium beam dissociation efficiency is 59% ± 1.3% and the oxygen beam is 25% ± 2.4%. The measured fluxes are 8.4×10^{12} atoms cm^{-2} s^{-1} (D), 2.9×10^{12} molecules cm^{-2} s^{-1} (D_2), 5.0×10^{11} atoms cm^{-2} s^{-1} (O), and 7.6×10^{11} molecules cm^{-2} s^{-1} (O_2) when flags are open and both choppers have 100% duty cycle. The plus-minus error is originated from day-to-day variations of the RF dissociation efficiencies. However, during a TPD run, the dissociation rates are stable.

In a typical experiment, the clean sample is held at low temperature and is singly exposed to the $^{18}O/^{18}O_2$ beam or simultaneously to the D/D_2 and $^{18}O/^{18}O_2$ beams. After the desired exposure time, the beam flux is cut off and the sample is heated to desorb surface species. The heating rate is 1 K s^{-1}. The QMS detector placed in front of the sample detects the desorbed materials and a TPD trace is generated.

3. RESULTS AND DISCUSSION

3.1. Thin Film Silicate Characterization. To obtain a deposition with characteristics similar to those of silicates, natural olivine samples were used as target in the EB-PVD. Energy dispersive X-ray (EDX) analysis and infrared spectroscopy show that the target is of forsterite in composition. EDX provides the analysis of the bulk stochiometric composition of the silicate samples whereas Fourier transform infrared spectroscopy gives information about adsorbates. EDX spectra are also obtained during the film growth at different thicknesses. Table 1 reports the abundance of different compounds obtained by EDX for the natural material used as target and the deposited thin film. A Bruker Hyperion 3000

Table 1. EDX Analysis of the Natural Olivine Used in the Evaporation Process and of the Thin Film Deposited on the Substrate

%	target	thin film
MgO	49	45
FeO	7	6
SiO_2	44	47

dx.doi.org/10.1021/jp312816k | J. Phys. Chem. A 2013, 117, 3009−3016

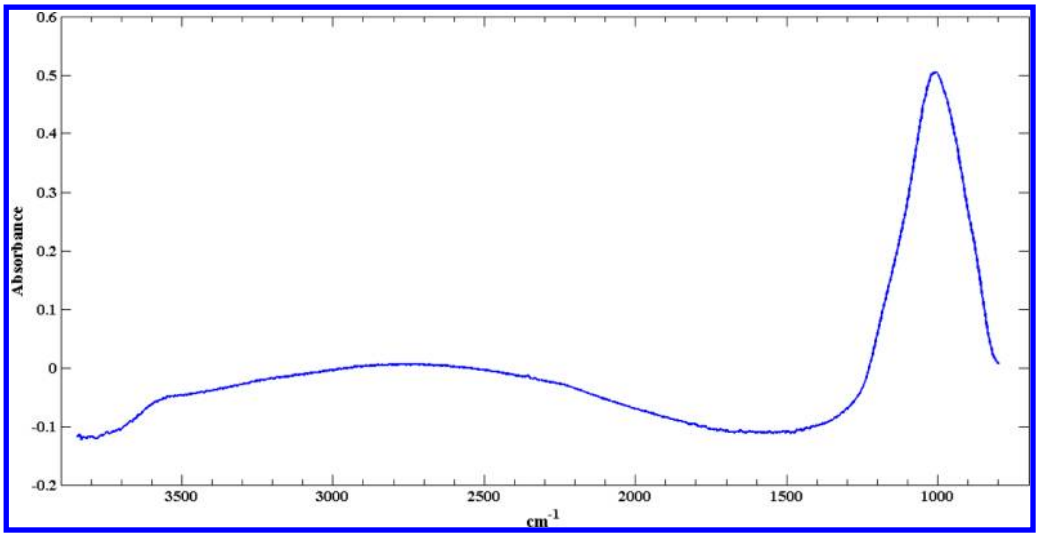

Figure 1. IR spectrum of the synthesized thin film silicate.

microscope is used with 4 cm^{-1} spectral resolution. Spectra are acquired after 64 scans on 6 different locations on the surface. The average spectrum after subtraction of the substrate background is shown in Figure 1. The intense band centered at 980 cm^{-1} is compatible with amorphous Mg-rich silicate. The EDX analysis indicates that the elemental composition of the target material is preserved during the EB-PVD process. Thus, thin film sample is amorphous silicate with composition of forsterite. The wide band ranging from 1500 to 3700 cm^{-1} is due to interference of the IR light going through the thin film in perpendicular direction. Isolated hydroxyl bonds are observed as freely vibrating OH stretching band at 3600 cm^{-1}. This single band is attributed to inert siloxane phase formed on the thin film surface, which is hydroxylated by OH radicals from the atmosphere.

Atomic force microscopy (AFM) images of the samples are also obtained to investigate the surface morphology. A Park Systems XE-100 microscope is used in contact mode. Root-mean-square roughness (R_q) is calculated as the average over several 25 μm^2 regions. A highly homogeneous morphology over several micrometers is observed (Figure 2). Submicrometric features, with lateral size ranging from ca. 100 nm up to 1 μm and heights of tens of nm are also observed (Figure 3). The roughness R_q of 2.8 nm highlights the presence of larger structures on the surface due to accretion process that occurs on preferential sites.

3.2. Surface Composition Modification by Ar^+ Sputtering. It is known that the surface chemical composition of many metal oxides can be modified by ion beam irradiation. Preferential sputtering of oxygen produces metal-rich surface layers.[24−26] One focus of this study is to investigate the surface compositional modification of amorphous silicate thin film caused by noble gas ion sputtering.

At first, we perform a benchmark TPD run prior to sputtering. The sample is exposed to the atomic oxygen beam for 30 min at 40 K. After exposure, the sample is first cooled to 10 K and subsequently heated to 150 K. The mass 36, $(^{18}O)_2$, signal is traced during heating. Two desorption peaks are observed: one small peak at 45 K and a large peak at 63 K (top trace in Figure 4a). The first peak is from the desorption of physisorbed oxygen molecules. At 40 K, most of the undissociated oxygen molecules are reflected by the surface.[27]

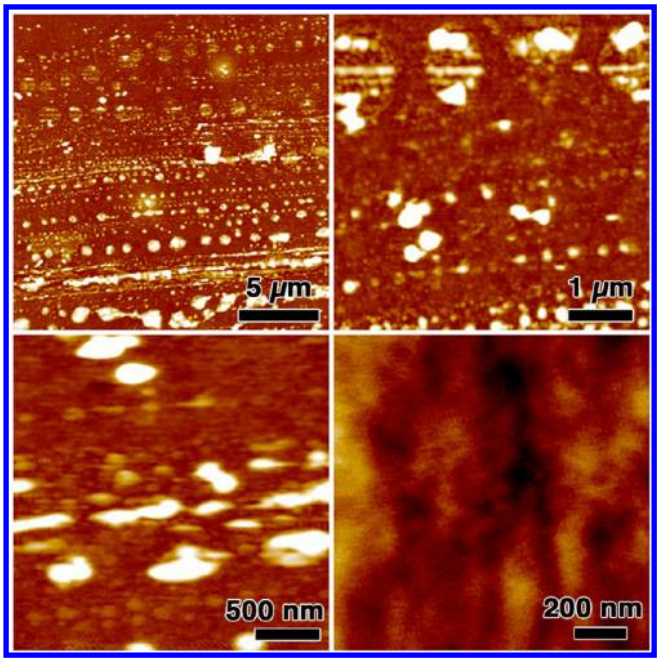

Figure 2. AFM images at different magnifications of the thin film sample. Height scale range is 20 nm in top-left image, 5 nm in the others.

However, a small fraction of the molecules will stay on the surface within the time frame of the experiment. The origin of the 63 K peak is 2-fold. First, O_2 molecules can be formed on the surface by collisions of diffusing O atoms. When two O atoms meet, they form an O_2 molecule that leaves the surface immediately. Second, one O atom can reactwith an O_2 molecule that is still on the surface due to the finite residence time to form O_3. The formation of O_3 is also observed from photodissociation of O_2 physisorbed on porous water ice at temperatures as high as 50 K.[28] The desorption of O_3 also contributes the mass 36 signal undertaking the ionization process listed below:

$$O_3 + e \rightarrow O_2^+ + O + 2e \quad (10)$$

The surface is then exposed to Ar^+ ion beam at 150 K. The ion energy is 3.5 keV and the ion flux is 7.5×10^{12} cm^{-2} s^{-1}.

dx.doi.org/10.1021/jp312816k | J. Phys. Chem. A 2013, 117, 3009−3016

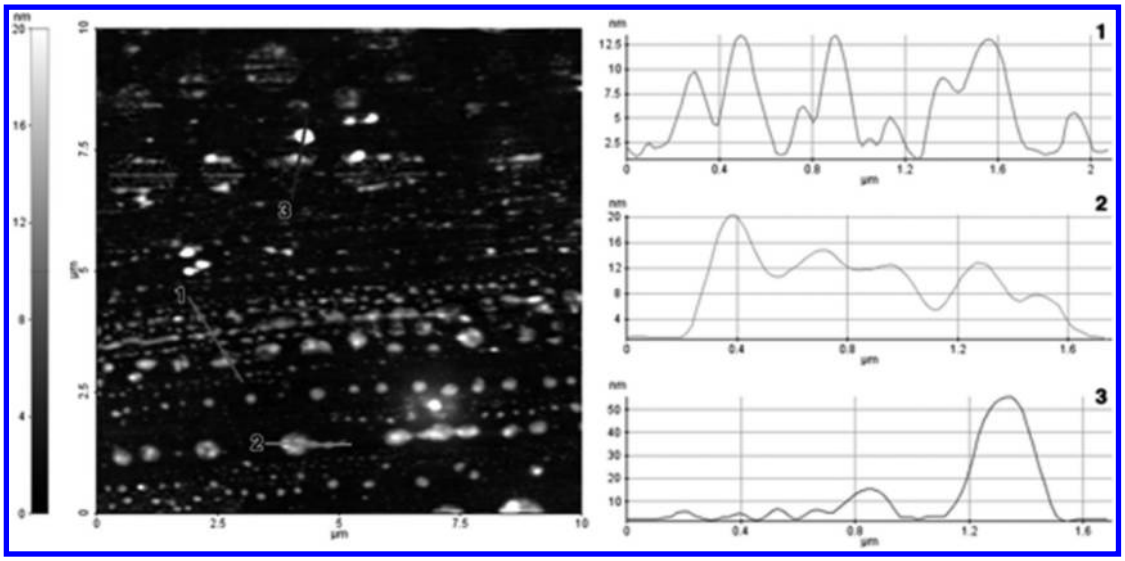

Figure 3. Height profile along selected lines in the AFM image.

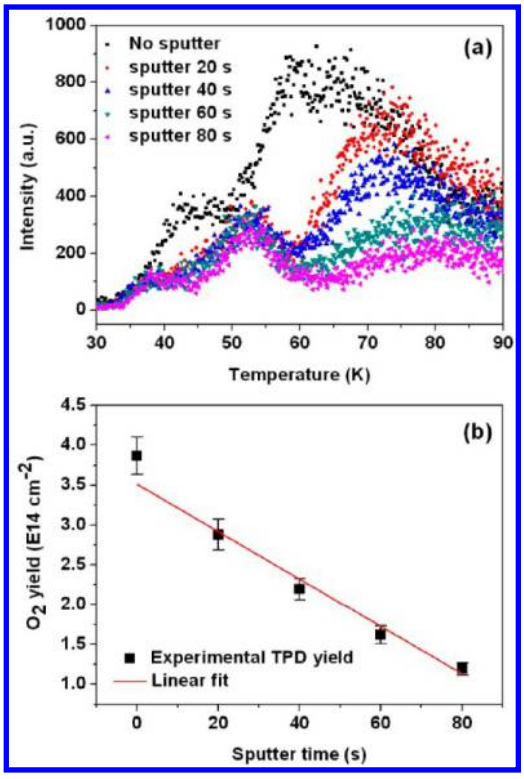

Figure 4. (a) O_2 TPD traces after 30 min of atomic oxygen exposure at 40 K. The sample has been sputtered for various lengths of time prior to oxygen exposure. After exposure, the sample is cooled to 10 K before the start of the TPD. (b) Experimental TPD yield from (a) and its linear fit as a function of sputter time.

The ion flux is estimated by using a Cu sputter target that has the same shape and area as the sample and is grounded via a picoammeter. After the desired sputter time, the same amount of atomic oxygen is deposited on the surface at 40 K and the same TPD procedure is followed as in the benchmark run. The TPD traces of O_2 desorption after various sputter times are similar to the benchmark run. However, two distinct changes can be observed. In Figure 4a, it first shows that the 45 K peak is shifted to 53 K. Peak area remains the same for all five TPD's. Second, as the sputter time increases, the second peak temperature increases but peak area decreases. The second peak is symmetrical and shifts to higher temperature indicating molecules are desorbing from deeper adsorption sites.This behavior can be understood by creation of surface oxygen vacancies induced by sputtering. Sputtering creates oxygen vacancies in the surface region and these vacancies can be filled by the deposited oxygen adatoms. Therefore, as sputtering dosage increases, more vacancy sites are created and more O atoms are consumed to fill these vacancies. Thus less atomic oxygen is left to form O_2 or O_3 during TPD.

The difference of the TPD yield between the benchmark and the sputtered runs is the amount of atomic oxygen used to fill the vacancy sites. We shall point out that the sputter-damaged surface can be restored in the fashion described above using atomic oxygen deposition. All the sputter-created vacancies are filled upon oxygen exposure. This is checked using water formation on the sputtered surface followed by oxygen treatment.[29] We performed water formation experiments using simultaneous D and O exposure at 8 K. On the oxygen treated sputtered surface, the same amount of D_2O is produced compared to the fresh, never sputtered surface. On the other hand, on the sputtered surface without oxygen treatment, less D_2O is formed due to the loss of oxygen used to fill the sputter-created vacancy sites (data not shown here). We are able to estimate the sputter rate given that all the sputter-created vacancies are filled upon oxygen exposure. Figure 4b shows the integrated peak area as a function of sputter time. The slope of the linear fit of the experiment data is proportional to the sputter rate. Its value is calculated to be 5.96×10^{12} cm^{-2} s^{-1}. Comparing the calculated experimental sputter rate to the ion flux, we estimate the sputter yield to be 0.8.

3.3. Water Formation on a Bare Silicate Surface. The second focus of this paper is water formation on a bare amorphous silicate surface at interstellar medium relevant temperatures. First, we study water adsorption on and desorption from the bare silicate surface and present a brief discussion on the water ice growth morphology on the surface. Heavy water $D_2{}^{16}O$ is purified by several freeze−thaw cycles before being delivered to the sample (held at 8 K) from one beamline with an 8° angle of incidence. Desorption peaks from three exposures are shown in Figure 5. Stacking of the TPD traces shows a single desorption peak ranging from 153 to 156

dx.doi.org/10.1021/jp312816k | J. Phys. Chem. A 2013, 117, 3009−3016

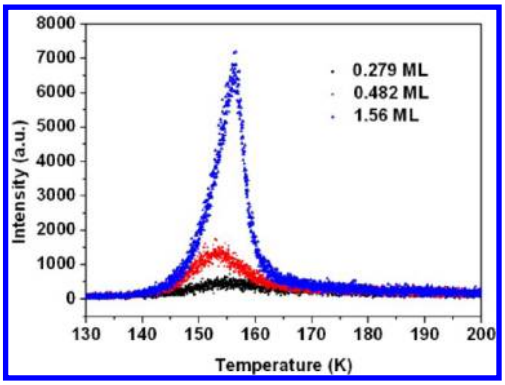

Figure 5. TPD traces for pure water ice desorption. Water ($D_2{}^{16}O$) is deposited from the beamline at 8 K.

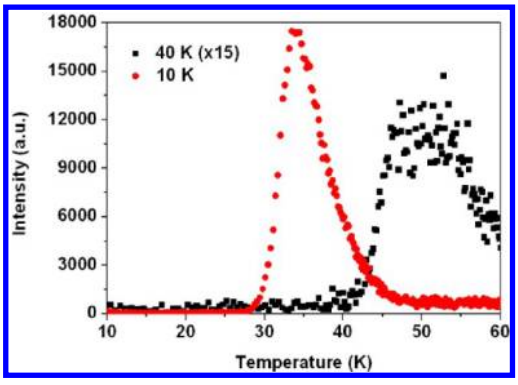

Figure 6. TPD traces after 10 min O_2 expsoure at 10 K (red circles) and 40 K (black squares). The 40 K exposure trace is rescaled by a factor of 15.

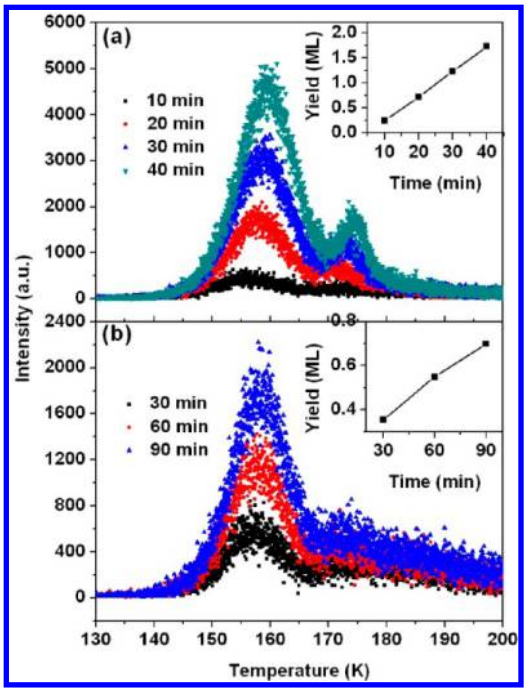

Figure 7. D_2O TPD traces after various simultaneous exposures of deuterium and oxygen at (a) 8 K and (b) 40 K. Oxygen beamline chopper duty cycle: 100%. Insets: integrated TPD yield of D_2O (after correction, see text) in units of monolayer coverage as a function of exposure time.

K as coverage increases. At the highest exposure (1.56 ML), shared leading edge and asymmetric peak shape suggest zeroth-order desorption kinetics, which points to a coverage independent sublimation of physisorbed water ice.[30] This desorption feature is different from water desorption from single crystal ZnO[31] and rutile TiO_2.[29] In these systems, water forms a chemisorbed first layer and ice grows on top. Therefore, TPD shows distinct peaks for the chemisorbed layer and ice layers. Moreover, it has been reported that water physisorbes and grows in 3D islands (i.e., Volmer–Weber growth mode) on highly oriented pyrolytic graphite at 90 K.[32] Our TPD data also suggest very similar growth behavior on an amorphous silicate surface. We interpret the peaks for small coverages (submonolayer regime) as desorption of water molecules from the first layer 2D islands. The peak for the highest coverage (multilayer regime) is assigned to desorption of water from 3D islands. Therefore, we propose that water physisorbes on the silicate surface and it follows the Volmer–Weber growth mode, forming 3D islands. Here we acknowledge that the water film is highly porous when deposited at 8 K,[33] although, as far as we know, the early stages of ice formation on these surfaces at low temperature (8 K) have not been studied. This may add complexity to the judgment of the growth mechanism. However, a detailed study of the growth and desorption behavior of pure water ice film is beyond the scope of this paper. Instead, we focus on the formation of water on amorphous silicate surface.

Next, we turn to the formation of water via hydrogenation of oxygen. In the present study, the atomic and molecular oxygen channels are investigated. We study the surface temperature and flux dependence of the two channels. At 8 K, both atomic and molecular oxygen have close to unity sticking on the surface.[34,35] Therefore the total reaction is a mixture of the two channels. At 40 K, most of the undissociated O_2 molecules are reflected from the surface.[27] Because of the finite residence time, about 6% of the O_2 molecules are detected to be on the surface at 40 K. This is experimentally determined by exposing the surface to molecular oxygen at 40 K, and then by comparing the TPD yield to the same amount of exposure at 8 K (Figure 6). Therefore, the atomic oxygen channel will dominate.

Experimental evidence for D_2O and D_2O_2 formation is presented below. Figures 7 and 8 show desorption of D_2O and D_2O_2 as a function of exposure time. Water desorption shows a large peak at 156 to 159 K and a small peak at 171 to 175 K for 8 K exposure. For the 40 K exposure, the small peak is not as pronounced as in the 8 K exposure and appears to be a shoulder of the large peak. As exposure time (coverage) increases, both peaks shift to higher temperatures. TPD spectra of D_2O_2 show that the desorption temperature is higher than that for D_2O. The peak temperature shifts from 171 to 174 K as the coverage increases. The stacking of the peaks also shows a typical zeroth-order desorption kinetics. Note that the small D_2O peak at ~170 K in Figure 7 resembles the D_2O_2 desorption peak and the peak temperatures overlap. However, the large D_2O peak (Figure 7) is broader and not as asymmetric as the D_2O_2 peak (Figure 8).

If we compare water desorption in Figure 5 to that in Figure 7, a couple of differences can be observed. The water formation TPD in Figure 7 split into two peaks and the lower temperature peak appears to be broader than molecular adsorbed water TPD in Figure 5. The observed peak broadening and splitting can be understood by the interactions between D_2O and D_2O_2 molecules formed on the surface. Wolff and coauthors[36] showed that layered CH_3OH and H_2O ice will mix upon

dx.doi.org/10.1021/jp312816k | J. Phys. Chem. A 2013, 117, 3009–3016

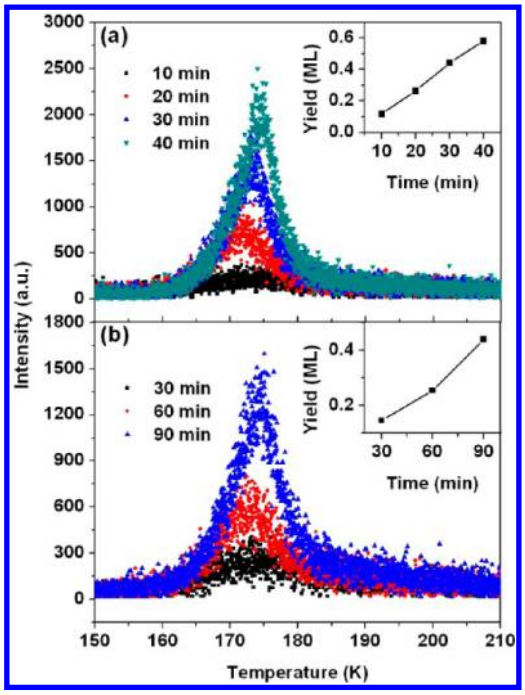

Figure 8. D_2O_2 TPD traces after various simultaneous exposures of deuterium and oxygen at (a) 8 K and (b) 40 K. Oxygen beamline chopper duty cycle: 100%. Insets: integrated TPD yield of D_2O_2 in units of monolayer coverage as a function of exposure time.

heating; as a result, water TPD peak broadens and an additional peak is observed. Burke et al.[37] showed a similar water TPD behavior in the layered C_2H_5OH/H_2O ice system. These observations are explained by an interaction of hydrogen bonding nature between water-like molecules (CH_3OH and C_2H_5OH) and water.[38,39] In our study, D_2O and D_2O_2 are believed to form during exposure rather than during TPD.[14,15] Upon heating, some of the D_2O molecules will mix with the D_2O_2 via hydrogen bonding and form an intimate mixture (a cluster of molecules) and the desorption of these D_2O molecules will be impeded by the presence of D_2O_2. These D_2O molecules will codesorb with D_2O_2 at 173 K, resulting in the higher temperature D_2O TPD peak. These clusters of mixed D_2O and D_2O_2 will also tend to hold the rest of the D_2O in place on the surface, resulting the broadening of the 150 K D_2O peak.

In Figure 9, we present water formation at 8 K for different values of the oxygen beam flux. It is reduced to 10% of its normal value by reducing the mechanical chopper duty cycle from 100% to 10%. This increases the D to O ratio by a factor of 10. In this experiment, only D_2O is observed. No D_2O_2 is detected. The absence of D_2O_2 is easily understood from reaction 5. When the D to O ratio is increased during simultaneous exposure, more excess atomic D is available for reaction 5 to take place. Therefore, D_2O_2 is depleted as a result. Because D_2O is the sole product in this experiment, no D_2O_2 is available to mix with D_2O and form an intimate mixture mentioned above; hence the D_2O desorption does not show peak broadening and splitting. In fact, it closely resembles the molecularly adsorbed water ice desorption shown in Figure 5.

Finally, we present quantitative analysis of the TPD data. We shall point out the challenge of using mass spectrometry to analyze D_2O_2 formation due to its poor stability and high reactivity. D_2O_2 is sensitive to surface decomposition, a number

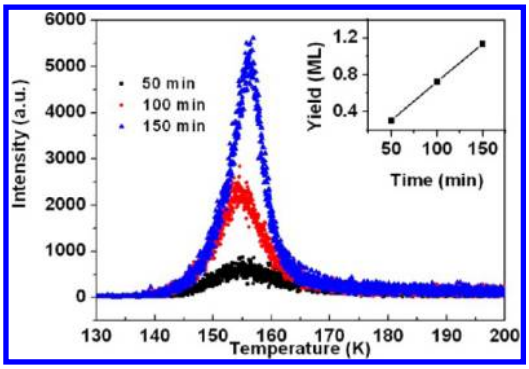

Figure 9. D_2O TPD traces after various simultaneous exposures of deuterium and oxygen at 8 K. Oxygen beamline chopper duty cycle: 10%. Inset: integrated TPD yield of D_2O in units of monolayer coverage as a function of exposure time.

of chemical species decomposed from pure hydrogen peroxide will enter the QMS detector if one tries to deliver it from a collimated molecular beamline.[40] Therefore, a pure sample of D_2O_2 mass spectrum is unavailable to calibrate our QMS detector. For that reason, we make a reasonable assumption that D_2O_2 has the same ionization efficiency as D_2O for our QMS detector. Also note that the ionization process of D_2O_2 is further complicated with significant amount of D_2O_2 undergoing various decomposition processes upon electron impact. One such process will affect the quantitative analysis of D_2O and D_2O_2 formation yields

$$D_2O_2 + e \rightarrow D_2O^+ + O + 2e \quad (11)$$

Because a pure sample of D_2O_2 is not available, an accurate estimation of the percentage of D_2O_2 undergoing the above decomposition process is unknown. Unfortunately, values reported from the literature are inconsistent.[40,41] Here we use the highest value (37 ± 3% D_2O^+ ion current compared to $D_2O_2^+$ ion current) to correct our experimental data. The corrected product yield represents an upper limit of D_2O_2 yield and a lower limit of D_2O yield.

Insets in Figure 7−9 show a linear increase in the formation of D_2O and D_2O_2 as a function of D and O exposure time in the time frame of our study. The coverage is calculated from the integrated desorption peak area followed by appropriate corrections mentioned above. The conversion factor from TPD peak area to monolayer (ML) coverage is obtained from the molecularly adsorbed water desorption experiment that also serves as a calibration. The amount of water deposited can be accurately calculated from beam flux and related to the TPD peak area to get the conversion factor. Here we define 1×10^{15} cm^{-2} as 1 ML. However, we do not assume there is wetting of the surface. The linear formation of products can also be expressed in terms of constant formation efficiency ε. The formation efficiency ε is the ratio of the number of oxygen nuclei in the product to the number of oxygen nuclei sent from the beam (including both O and O_2; note that the sticking coefficient is not factored in). An ε value of 1 means all the oxygen nuclei sent from the beam are used to form the product and an ε value of 0 means no such product is formed (no oxygen is consumed to form this product). Therefore, it is clear that ε is a measure of the reaction efficiency. The ε values for D_2O and D_2O_2 in different exposure scenarios are summarized in Table 2.

dx.doi.org/10.1021/jp312816k | J. Phys. Chem. A 2013, 117, 3009−3016

Table 2. Formation Efficiency ϵ for D_2O and D_2O_2 and Their Relative Yield in Different Exposure Scenarios

				formation efficiency ϵ		relative yield
O-line duty	D/O ratio	D/O_2 ratio	Temp (K)	D_2O	D_2O_2	D_2O:D_2O_2
100%	17	11	8	0.301 ± 0.068	0.224 ± 0.024	(2.7 ± 0.7):1
			40	0.079 ± 0.017	0.077 ± 0.006	(2.0 ± 0.5):1
10%	170	110	8	0.577 ± 0.065	0	∞
			40	0.174	0	∞

From Table 2, several points can be made. (1) In any scenario investigated, D_2O has a larger yield than D_2O_2. (2) When molecular oxygen is involved in the reaction network, D_2O_2 acts as an intermediate product. Increasing the D to O ratio will drive reaction 5 to the right-hand side converting D_2O_2 into D_2O. In fact, when the D to O ratio increases by a factor of 10, D_2O_2 is completely depleted. (3) Both D_2O and D_2O_2 formation efficiencies decrease as surface temperature increases. This is not surprising as the higher the surface temperature, the lower the sticking coefficient for both D and O. However, the D_2O/D_2O_2 ratio increases as the surface temperature increases. Our observations of formation of D_2O and D_2O_2 are similar to what has been obtained by Oba et al.[42] In their codeposition of H and O_2 on an Al substrate at 10−40 K studies, they observed the H_2O/H_2O_2 ratio increases with increasing H/O_2 ratio. The H_2O/H_2O_2 ratio also increases when the surface temperature is increased from 10 to 20 K.

At last, we briefly comment on the reaction network for D_2O and D_2O_2 formation. In our experiment, D_2O_2 can be formed via reactions 4 ($DO_2 + D \rightarrow D_2O_2$) and 7 ($OD + OD \rightarrow D_2O_2$). Reaction 4 is the second step of hydrogenation of O_2. This reaction, the same as its previous step , is barrierless.[21] Reaction 7 was studied by Oba et al. at 40−60 K. This radical−radical reaction is also barrierless and is the predominant route for H_2O_2 formation in their study.[20] In our study OD can be formed in a number of ways, including reaction of D with O_3, see reaction 6 above. We believe both reactions 4 and 7 contribute to the D_2O_2 formation in our study. However, as temperature increases from 8 to 40 K, the relative weight of reaction 4 decreases as the sticking of O_2 decreases dramatically (Figure 6). The fact that the yield of D_2O_2 does not drop as dramatically as the O_2 sticking confirms the occurrence of reaction 7. D_2O can be formed via reactions 2 ($OD + D \rightarrow D_2O$), 5 ($D_2O_2 + D \rightarrow D_2O + OD$), 8 ($OD + OD \rightarrow D_2O + O$), and 9 ($OD + D_2 \rightarrow D_2O + D$). The radical−radical reactions 2 and 8 are barrierless.[21] Reaction 5 has a gas-phase reaction barrier of 2000 K. However, this reaction, on the surface, is expected to have a detectable efficiency evidenced by the disappearance of D_2O_2 when the D to O ratio is increased by a factor of 10. The D_2O_2 formed is totally consumed through reaction 5 in the presence of excess atomic D. Reaction 9 has a gas-phase reaction barrier of 2100 K, but it can proceed on a cold surface through quantum tunneling.[21] This reaction also has a significant isotope effect, which shows that $OD + H_2 \rightarrow HDO + H$ is about 1 order of magnitude more efficient than $OD + D_2 \rightarrow D_2O + D$.[21] In our study, we observed HDO formation at 10 K using only O and D exposure (data not shown). This is explained by the formation of OD and its further reaction with H_2 adsorbed from the UHV background at 10 K. This observation confirms the occurrence (probably through quantum tunneling) of reaction 9 with H_2. However, in the current study, it is not possible to measure the efficiency of reaction 9 with D_2 to form D_2O.

4. CONCLUSIONS

The study of the initial stages of formation of water on silicate surfaces at low temperature poses unique challenges compared to the study of water formation on oxides and metals. Because of the weak interaction of reactants with the surface and the fast diffusion of hydrogen, the network of reactions is particularly complex. By exploiting the observation that at 40 K molecular oxygen is depleted, but not atomic oxygen, and by changing the D/O ratio, we were able to show the following: (1) At 8 K, both reactions ($DO_2 + D \rightarrow D_2O_2$) and ($OD + OD \rightarrow D_2O_2$) operate, but then at 40 K, because the coverage of O_2 is greatly diminished, only the OD + OD reaction is viable. (2) At both temperatures, the net yield of D_2O_2 is suppressed as the D/O ratio is increased 10-fold. Thus, these experiments point to the reason why in interstellar space D_2O_2 is detected at such low abundance.[22]

AUTHOR INFORMATION

Corresponding Author

*Tel: 315-443-9115.

Notes

The authors declare no competing financial interest.

ACKNOWLEDGMENTS

This work is supported by the NSF, Astronomy & Astrophysics Division (Grant No. 0908108), NASA (Grant No. NNX12AF38G), and by MIUR PRIN-08.

REFERENCES

(1) Pauer, G.; Winkler, A. Water Formation on Pd(111) by Reaction of Oxygen with Atomic and Molecular Hydrogen. *J. Chem. Phys.* **2004**, *120*, 3864−70.

(2) Mitsui, T.; Rose, M. K.; Fomin, E.; Ogletree, D. F.; Salmeron, M. A Scanning Tunneling Microscopy Study of the Reaction between Hydrogen and Oxygen to Form Water on Pd(111). *J. Chem. Phys.* **2002**, *117*, 5855−5858.

(3) Nagasaka, M.; Kondoh, H.; Amemiya, K.; Nambu, A.; Nakai, I.; Shimada, T.; Ohta, T. Mechanism of Water Formation on Pt(111) Revealed by Time-Resolved NEXAFS Experiment and Kinetic Monte Carlo Simulation. *Hyomen Kagaku* **2005**, *26*, 378−384.

(4) Gustafsson, K.; Andersson, S. Infrared Spectroscopy of Oxygen Adsorbed on Hydrogen Covered Pt(111). *J. Chem. Phys.* **2004**, *121*, 8532−8536.

(5) Monine, M. I.; Schaak, A.; Rubinstein, B. Y.; Imbihl, R.; Pismen, L. M. Dynamics of Subsurface Oxygen Formation in Catalytic Water Formation on a Rh(111) Surface - Experiment and Simulation. *Catal. Today* **2001**, *70*, 321−330.

(6) Africh, C.; Lin, H.; Corso, M.; Esch, F.; Rosei, R.; Hofer Werner, A.; Comelli, G. Water Production Reaction on Rh(110). *J. Am. Chem. Soc.* **2005**, *127*, 11454−11459.

(7) Kratzer, M.; Surnev, S.; Netzer, F. P.; Winkler, A. Model Reaction Studies on Vanadium Oxide Nanostructures on Pd(111). *J. Chem. Phys.* **2006**, *125*, 074703/1−9.

(8) Kratzer, M. J.; Stettner, J.; Winkler, A. Water Formation on Clean and Vanadium Oxide Covered Pd(111) by Permeating Deuterium. *J. Phys. Chem. C* **2007**, *111*, 12723−12729.
(9) Whittet, D. C. B.; Tielens, A. G. G. M. Infrared Observations of Interstellar Dust Absorption Features. *Astron. Soc. Pacific Conf. Ser.* **1997**, *122*, 161−178.
(10) Williams, D. A.; Brown, W. A.; Price, S. D.; Rawlings, J. M. C.; Viti, S. Interstellar Molecules. *Astron. Geophys.* **2007**, *48*, 1.25−1.34.
(11) d'Hendecourt, L. B.; Allamandola, L. J.; Greenberg, J. M. Time-Dependent Chemistry in Dense Molecular Clouds 0.1. Grain Surface-Reactions, Gas Grain Interactions and Infrared-Spectroscopy. *Astron. Astrophys.* **1985**, *152*, 130−150.
(12) Hasegawa, T. I.; Herbst, E.; Leung, C. M. Models of Gas-Grain Chemistry in Dense Interstellar Clouds with Complex Organic-Molecules. *Astrophys. J. Suppl. Ser.* **1992**, *82*, 167−195.
(13) Tielens, A.; Hagen, W. Model-Calculations of the Molecular Composition of Interstellar Grain Mantles. *Astron. Astrophys.* **1982**, *114*, 245−260.
(14) Dulieu, F.; Amiaud, L.; Congiu, E.; Fillion, J. H.; Matar, E.; Momeni, A.; Pirronello, V.; Lemaire, J. L. Experimental Evidence for Water Formation on Interstellar Dust Grains by Hydrogen and Oxygen Atoms. *Astron. Astrophys.* **2010**, *512*, A30.
(15) Jing, D.; He, J.; Brucato, J.; De Sio, A.; Tozzetti, L.; Vidali, G. On Water Formation in the Interstellar Medium: Laboratory Study of the O+D Reaction on Surfaces. *Astrophys. J. Lett.* **2011**, *741*, L9.
(16) Miyauchi, N.; Hidaka, H.; Chigai, T.; Nagaoka, A.; Watanabe, N.; Kouchi, A. Formation of Hydrogen Peroxide and Water from the Reaction of Cold Hydrogen Atoms with Solid Oxygen at 10 K. *Chem. Phys. Lett.* **2008**, *456*, 27−30.
(17) Ioppolo, S.; Cuppen, H. M.; Romanzin, C.; van Dishoeck, E. F.; Linnartz, H. Water Formation at Low Temperatures by Surface O_2 Hydrogenation I: Characterization of Ice Penetration. *Phys. Chem. Chem. Phys.* **2010**, *12*, 12065−12076.
(18) Mokrane, H.; Chaabouni, H.; Accolla, M.; Congiu, E.; Dulieu, F.; Chehrouri, M.; Lemaire, J. L. Experimental Evidence for Water Formation via Ozone Hydrogenation on Dust Grains at 10 K. *Astrophys. J. Lett.* **2009**, *705*, L195.
(19) Romanzin, C.; Ioppolo, S.; Cuppen, H. M.; van Dishoeck, E. F.; Linnartz, H. Water Formation by Surface O_3 Hydrogenation. *J. Chem. Phys.* **2011**, *134*, 084504.
(20) Oba, Y.; Watanabe, N.; Kouchi, A.; Hama, T.; Pirronello, V. Experimental Studies of Surface Reactions among OH Radicals that Yield H_2O and CO_2 at 40−60 K. *Phys. Chem. Chem. Phys.* **2011**, *13*, 15792−15797.
(21) Oba, Y.; Watanabe, N.; Hama, T.; Kuwahata, K.; Hidaka, H.; Kouchi, A. Water Formation through a Quantum Tunneling Surface Reaction, OH + H_2, at 10 K. *Astrophys. J.* **2012**, *749*, 67/1−12.
(22) Bergman, P.; Parise, B.; Liseau, R.; Larsson, B.; Olofsson, H.; Menten, K. M.; Gusten, R. Detection of Interstellar Hydrogen Peroxide. *Astron. Astrophys.* **2011**, *531*, L8.
(23) Roser, J. E.; Vidali, G.; Manico, G.; Pirronello, V. Formation of Carbon Dioxide by Surface Reactions on Ices in the Interstellar Medium. *Astrophys. J.* **2001**, *555*, L61.
(24) Chung, Y. W.; Lo, W. J.; Somorjai, G. A. Low Energy Electron Diffraction and Electron Spectroscopy Studies of the Clean (110) and (100) Titanium Dioxide (Rutile) Crystal Surfaces. *Surf. Sci.* **1977**, *64*, 588−602.
(25) Jech, C.; Kelly, R. Studies on Bombardment-Induced Disorder. I. Gas-Release Study of the Annealing of Bombardment-Induced Disorder. *J. Phys. Chem. Solids* **1969**, *30*, 465−474.
(26) Mizutani, T. Compositional and Structural Modifications of Amorphous SiO_2 by Low-Energy Ion and Neutral Beam Irradiation. *J. Non-Cryst. Solids* **1995**, *181*, 123−134.
(27) Jing, D.; He, J.; Brucato, J. R.; Vidali, G.; Tozzetti, L.; De sio, A. Formation of Molecular Oxygen and Ozone on Amorphous Silicates. *Astrophys. J.* **2012**, *756*, 98.
(28) Shi, J.; Raut, U.; Kim, J. H.; Loeffler, M.; Baragiola, R. A. Ultraviolet Photon-Induced Synthesis and Trapping of H_2O_2 and O_3 in Porous Water Ice Films in the Presence of Ambient O_2: Implications for Extraterrestrial Ice. *Astrophys. J. Lett.* **2011**, *738*, L3.
(29) Zehr, R. T.; Henderson, M. A. Influence of O_2-Induced Surface Roughening on the Chemistry of Water on TiO_2(110). *Surf. Sci.* **2008**, *602*, 1507−1516.
(30) Henderson, M. A. The Interaction of Water with Solid Surfaces: Fundamental Aspects Revisited. *Surf. Sci. Rep.* **2002**, *46*, 5−308.
(31) Zwicker, G.; Jacobi, K. Site-Specific Interaction of Water with Zinc Oxide Single-Crystal Surfaces Studied by Thermal Desorption and UV Photoelectron Spectroscopy. *Surf. Sci.* **1983**, *131*, 179−194.
(32) Bolina, A. S.; Wolff, A. J.; Brown, W. A. Reflection Absorption Infrared Spectroscopy and Temperature-Programmed Desorption Studies of the Adsorption and Desorption of Amorphous and Crystalline Water on a Graphite Surface. *J. Phys. Chem. B* **2005**, *109*, 16836−16845.
(33) Kimmel, G. A.; Stevenson, K. P.; Dohnalek, Z.; Smith, R. S.; Kay, B. D. Control of Amorphous Solid Water Morphology Using Molecular Beams. I. Experimental Results. *J. Chem. Phys.* **2001**, *114*, 5284−5294.
(34) Acharyya, K.; Fuchs, G. W.; Fraser, H. J.; van Dishoeck, E. F.; Linnartz, H. Desorption of CO and O_2 Interstellar Ice Analogs. *Astron. Astrophys.* **2007**, *466*, 1005−U169.
(35) Fuchs, G. W.; Acharyya, K.; Bisschop, S. E.; Oberg, K. I.; van Broekhuizen, F. A.; Fraser, H. J.; Schlemmer, S.; van Dishoeck, E. F.; Linnartz, H. Comparative Studies of O_2 and N_2 in Pure, Mixed and Layered CO Ices. *Faraday Discuss* **2006**, *133*, 331−345.
(36) Wolff, A. J.; Carlstedt, C.; Brown, W. A. Studies of Binary Layered CH_3OH/H_2O Ices Adsorbed on a Graphite Surface. *J. Phys. Chem. C* **2007**, *111*, 5990−5999.
(37) Burke, D. J.; Wolff, A. J.; Edridge, J. L.; Brown, W. A. Thermally Induced Mixing of Water Dominated Interstellar Ices. *Phys. Chem. Chem. Phys.* **2008**, *10*, 4956−67.
(38) Thierfelder, C.; Schmidt, W. G. Ethanol Adsorbed on Ice: A First-Principles Study. *Phys. Rev. B* **2007**, *76*, 195426.
(39) Peybernes, N.; Le Calve, S.; Mirabel, P.; Picaud, S.; Hoang, P. N. M. Experimental and Theoretical Adsorption Study of Ethanol on Ice Surfaces. *J. Phys. Chem. B* **2004**, *108*, 17425−17432.
(40) Tessier, A.; Forst, W. Kinetics of Hydrogen Peroxide Pyrolysis by Molecular-Beam Mass Spectrometry. *Int. J. Mass Spectrom. Ion Phys.* **1971**, *7*, 281−295.
(41) Foner, S. N.; Hudson, R. L. Ionization and Dissociation of Hydrogen Peroxide by Electron Impact. *J. Chem. Phys.* **1962**, *36*, 2676−2680.
(42) Oba, Y.; Miyauchi, N.; Hidaka, H.; Chigai, T.; Watanabe, N.; Kouchi, A. Formation of Compact Amorphous H_2O Ice by Codeposition of Hydrogen Atoms with Oxygen Molecules on Grain Surfaces. *Astrophys. J.* **2009**, *701*, 464−470.